

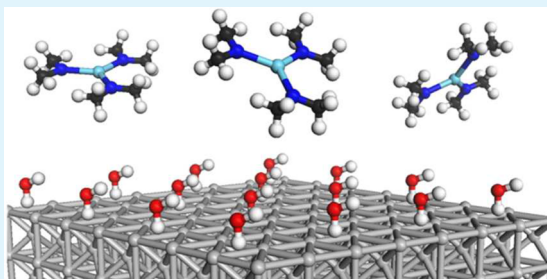
Density Functional Theory Predictions of the Composition of Atomic Layer Deposition-Grown Ternary Oxides

Ciaran Murray and Simon D. Elliott*

Tyndall National Institute, University College Cork, Dyke Parade, Cork, Ireland

S Supporting Information

ABSTRACT: The surface reactivity of various metal precursors with different alkoxide, amide, and alkyl ligands during the atomic layer deposition (ALD) of ternary oxides was determined using simplified theoretical models. Quantum chemical estimations of the Brønsted reactivity of a metal complex precursor at a hydroxylated surface are made using a gas-phase hydrolysis model. The geometry optimized structures and energies for a large suite of 17 metal precursors (including cations of Mg, Ca, Sr, Sc, Y, La, Ti, Zr, Cr, Mn, Fe, Co, Ni, Cu, Zn, Al, and Ga) with five different anionic ligands (conjugate bases of *tert*-butanol, tetramethyl heptanedione, dimethyl amine, isopropyl amidine, and methane) and the corresponding hydrolyzed complexes are calculated using density functional theory (DFT) methods. The theoretically computed energies are used to determine the energetics of the model reactions. These DFT models of hydrolysis are used to successfully explain the reactivity and resulting stoichiometry in terms of metal cation ratios seen experimentally for a variety of ALD-grown ternary oxide systems.



KEYWORDS: atomic layer deposition, density functional theory, ternary oxides, stoichiometry, metal precursors, ligand

1. INTRODUCTION

Ternary oxides ($M^1_x M^2_{1-x} O_y$) are a large class of functional materials (including the well-known perovskites with ABO_3 structures¹) which have produced much interest due to their potential in a wide-range of technological applications. The properties of these materials are dependent on the ratios of metal cations in their structures. Atomic layer deposition (ALD)² has been applied successfully in the growth of high quality thin films of binary oxides ($M^1 O_x$)^{3–6} and is seen as a potential method for depositing nanoscale ternary oxide ($M^1 M^2 O_x$) structures with controlled stoichiometries. ALD ternary oxide thin films are produced in a similar manner to binary oxides: a substrate is exposed to a metal precursor containing metal M^1 within an ALD reactor for a set pulse time allowing a coating of the precursor to form; the ALD reactor is then purged/evacuated to remove excess metal precursor; after purging, a second precursor pulse occurs where an oxygen source (e.g., ozone) is allowed to flow into the reactor, removing the remaining ligands. This cycle is repeated n_1 times until a sufficient amount of $M^1 O_x$ is deposited. This is followed by n_2 cycles using a different metal precursor containing M^2 and an appropriate oxygen source (which could be different, e.g., water), depositing $M^2 O_x$ and creating an $M^1 M^2 O_x$ thin film. The $M^1 + M^2$ supercycle is repeated until a desired $M^1 M^2 O_x$ film thickness is achieved.

Film composition of $M^1 M^2 O_x$ solids have been found to depend in a consistent but nonlinear way on the ALD pulse ratios, $P(M^1) = n_1 / (n_1 + n_2)$, revealing differences between the chemistry of the two metal precursors.^{7,8} From the application of a “Surface Utilization Model” to the resulting stoichiometries

of a series of ternary oxides produced using β -diketonate metal precursors, the fraction of ligands eliminated by Brønsted reactions in the metal pulse before the O_3 pulse is found to be strongly dependent on the identity of the pair of metal cations in the particular ternary oxide.⁸ However, the surface utilization model could not account for some experimental stoichiometries (e.g., $LaMnO_x$, $CaMnO_x$, and $CoFeO_x$), which suggests that more complex surface chemistry is at play. In this study we extend the model and attempt to account for the resulting stoichiometries of a series of metal precursors that have been combined pairwise in thermal ALD by determining the relative reactivities of these precursors toward ligand elimination. The reactivity of the precursors affects the deposition rates of individual metal cations and hence the final composition of the ternary oxide.

Two mechanisms have been proposed for the nonlinear growth of ternary oxides using the ALD of organo-metallic precursors combined pairwise followed by oxidation with ozone or oxygen plasma.⁸ Mechanism A assumes no elimination of the surface-bound ligands before the oxidizing pulse (either because the ligands are inert or because there are no surface hydroxyl groups), followed by removal of all ligands via combustion. This leads to an expression for the final stoichiometry of the oxide layer that is simply dependent on the number of precursor pulses, n , and the charge of the metal cation, q .

Received: January 23, 2013

Accepted: April 1, 2013

Published: April 1, 2013

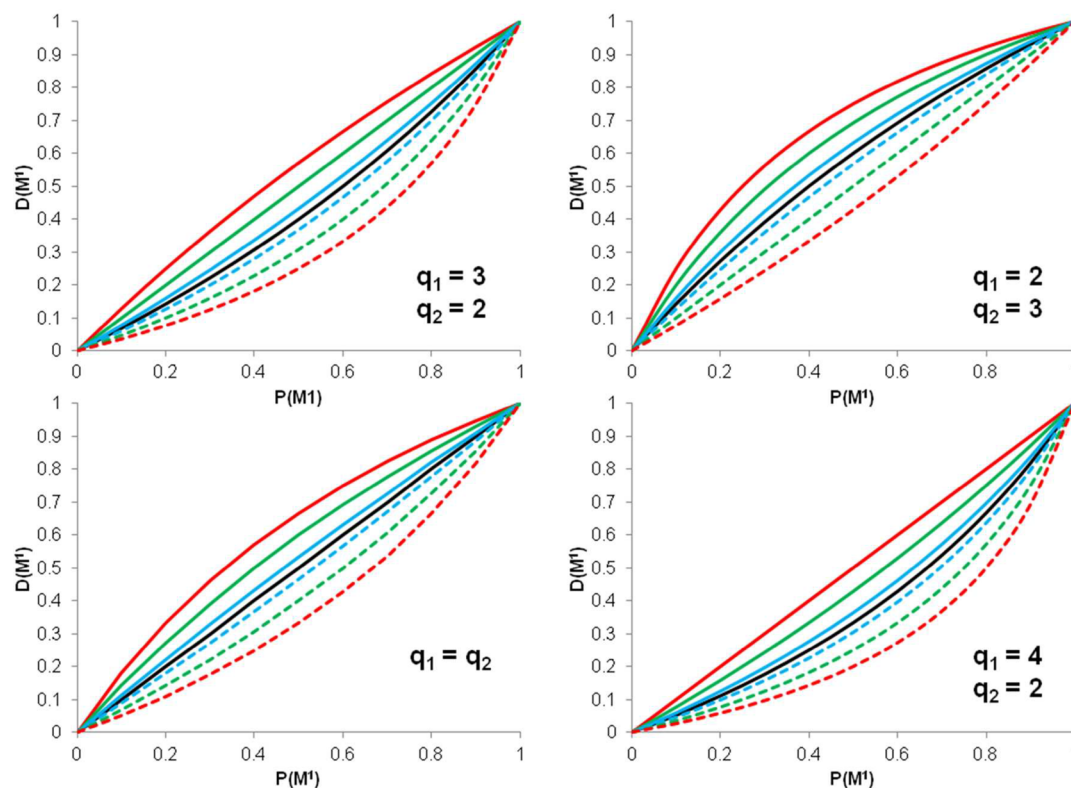


Figure 1. Predicted ratios of M^1 ions in $M^1M^2O_x$ ternary oxide, $D(M^1)$, as a function of the M^1 pulse ratio, $P(M^1)$, with different ionic charges, q_1 and q_2 . The ratios predicted using mechanism A (eq 1) are shown in black. The compositions predicted using Mechanism B (eq 2) with higher ratios of Bronsted eliminated M^1 ligands compared to M^2 are shown by the solid blue (3:2), green (4:1), and red (1:0) curves while those with lower ratios of M^1 ligands eliminated are shown by the dashed blue (2:3), green (1:4), and red (0:1) curves.

$$D_1^A = (n_1/q_1)/[(n_1/q_1) + (n_2/q_2)] \quad (1)$$

There is no fitting to experimental data for mechanism A. We note that, as shown in Figure 1, D^A is a linear function of pulse ratio only if $q_1 = q_2$.

Mechanism B makes the assumption that hydroxyl groups remain on the surface from previous oxidation steps.⁹ These may then act as a source of protons and allow a fraction of the ligands to be eliminated before combustion, thus permitting more metal precursor to be deposited. Therefore in mechanism B (Figure 1), the growth rate of a metal oxide and stoichiometry of the thin film are additionally dependent on the fraction of ligands eliminated by combination with protons available on the surface, f , which is obtained by attempting to fit D^B to the experimental data

$$D_1^B = (n_1(f_1 + 1)/q_1)/[(n_1(f_1 + 1)/q_1) + (n_2(f_2 + 1)/q_2)] \quad (2)$$

A third mechanism that may affect the ALD growth rate of a metal oxide and influence the resulting ternary oxide composition is a ligand exchange process. In this proposed mechanism C, a rapid exchange of ligands may occur from an adsorbed M^1 metal precursor to an M^2 metal cation at the growing oxide surface. Ligand elimination via mechanism B may then be considered not from M^1 but from M^2 to which the ligand is now bonded. We suggest that mechanism C explains cases where neither mechanism B nor mechanism A fully account for experimental stoichiometries.

Quantum chemical and in particular density functional theory (DFT) calculations offer a convenient and reliable way

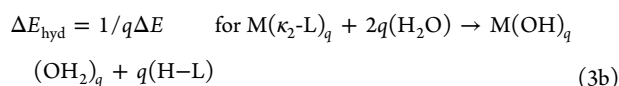
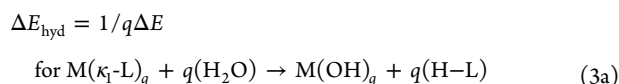
of predicting many experimentally measurable chemical properties of the majority of main-group element molecules, e.g. molecular geometries and vibrational frequencies.¹⁰ Calculations involving transition metal complexes are susceptible to errors in electronic exchange and correlation and careful selection of the DFT functional is important to ensure accurate geometries^{11–13} and reaction enthalpies.¹⁴ ALD surface chemistries may be accurately described by explicitly modeling the atomic structure of a given oxide using, for example, slab calculations with periodic boundary conditions. This is so time-consuming that it has been carried out for only a small selection of binary oxides so far.¹⁵ Instead, the approach taken here is to study a simple gas-phase model that describes the bond making and bond breaking essential to the surface reactions of interest,¹⁶ thus allowing a larger number of chemical systems to be considered.^{17,18} The model takes no account of surface geometry or reaction pathways, other than the possibility of proton transfer (mechanism B) and ligand exchange (mechanism C).

We present here the potential ALD metal complexes $M(L)_q$ where M is a metal cation with a charge q of +2, +3, or +4 and L is an anionic ligand with a -1 charge. Seventeen metals in total were examined: 7 $M(II)$ cations ($M = Mg, Ca, Sr, Co, Ni, Cu$ or Zn), 8 $M(III)$ cations ($M = Sc, Y, La, Cr, Mn, Fe, Al$ or Ga), and 2 $M(IV)$ cations (Ti or Zr). The ligands considered include two that bond via oxygen namely, *tert*-butanolate, O^tBu [$OC(CH_3)_3$], and the β -diketonate thd [$2,2,6,6$ -tetramethylheptane-3,5-dionate], two that bond via nitrogen namely, dimethyl amide, dma [$N(CH_3)_2$] and the isopropyl amidinate amd [$R^1NC(R^2)NR^1$ with $R^1 = ^iPr = C(CH_3)_2$ and $R^2 = CH_3$] and one alkyl, methyl (CH_3). These ligands may be grouped

not only by their coordinating atoms (O, N, and C) but also by their denticity where O^tBu, dma, and CH₃ are monodentates (κ_1) and thd and amd are bidentates (κ_2). It is appreciated that many of the complexes presented in this work are experimentally unviable due to unstable M–L bonds or steric hindrance at coordination sites but are included for completeness. A simple model for the elimination and exchange of precursor ligands by reaction with surface groups will be presented in sections 2.1 and 2.2, and thermodynamic energies for these reactions determined using DFT in sections 3.3, 3.4, and 3.5. The DFT results will be compared in section 4 to experimental results in the literature and in particular to those in ref 8, where the reaction mechanisms proposed using the surface utilization model for the deposition of ternary oxides using M(thd)_q metal precursors will be assessed.

2. COMPUTATIONAL METHOD

2.1. Gas-Phase Hydrolysis Model. As a model for the elimination of H–L from the surface, the gas-phase energetics for the hydrolysis of M(L)_q may be calculated using quantum chemical methods.^{17,18}



In eqs 3a and 3b, ΔE is quoted per ligand to allow comparison between the different ML₂, ML₃, and ML₄ complexes. A more negative ΔE_{hyd} value corresponds to a more exothermic hydrolysis reaction and a greater possibility of H–L elimination. As this model is concerned solely with the changes in bonding, temperature effects are neglected. In this model H₂O represents the source of hydroxyl groups on the surface while the substitution of OH groups for the ligands models the formation of M–O bonds in the solid (Figure 2). We stress that

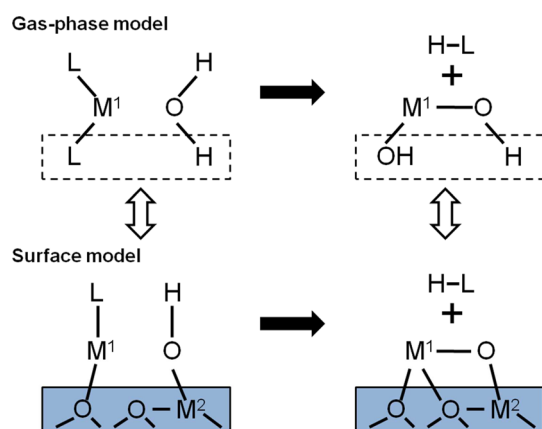


Figure 2. Representation of gas-phase hydrolysis (top) as a model for Brønsted elimination of ligand from ALD precursor at a surface (bottom).

although H₂O appears in the calculations, the mechanisms assume ALD with an oxidizing coreagent such as ozone or oxygen plasma. In order to negate the effects from the change in coordination number for ligands of higher denticity (e.g., κ_2), the energies for the hydrated complexes M(OH)_q(OH₂)_q have been calculated rather than M(OH)_q for the monodentate ligands (κ_1). The extent to which H–L is eliminated will therefore depend on the free energy change for the hydrolysis reaction, ΔE_{hyd} .

ΔE_{hyd} may be separated into two factors. The first factor is the Brønsted basicity (BB) of L[−] relative to OH[−] in forming the neutral H–L molecule and is given by

$$\Delta E_{\text{BB}} = \Delta E \quad \text{for } L^- + \text{H}_2\text{O} \rightarrow \text{H-L} + \text{OH}^- \quad (4)$$

This factor is used to compare the Brønsted basicity of the ligands, i.e. the more negative ΔE_{BB} , the stronger the BB of the ligand anion. The second factor is the Lewis basicity (LB) of L[−] relative to OH[−] in forming adducts with a particular metal:

$$\Delta E_{\text{LB}} = 1/q\Delta E$$

$$\text{for } M(\text{OH})_q + q(L^-) \rightarrow M(\kappa_1\text{-L})_q + q(\text{OH}^-) \quad (5a)$$

$$\Delta E_{\text{LB}} = 1/q\Delta E$$

$$\text{for } M(\text{OH})_q(\text{OH}_2)_q + q(L^-) \rightarrow M(\kappa_2\text{-L})_q + q(\text{OH}^-)$$

$$+ q(\text{H}_2\text{O}) \quad (5b)$$

The more exothermic the ΔE_{LB} , the more stable the ML_q compared to M(OH)_q and the less likely M^{q+} is to form M–O bonds. Comparing the expressions for hydrolysis and Brønsted and Lewis basicity, it is clearly seen that $\Delta E_{\text{hyd}} = \Delta E_{\text{LB}} - \Delta E_{\text{BB}}$, i.e. the tendency to eliminate ligands is due to the difference in ligand basicity for M^{q+} and H⁺. Consequently, the more negative ΔE_{BB} is relative to ΔE_{LB} , the more likely it is for H–L to be eliminated from ML_q.

2.2. Ligand Exchange Model. Another possible reaction that may influence the growth rate is the exchange of a ligand from an incoming or adsorbed M¹L_q complex with pre-existing M² metal ions at the growing oxide surface (Figure 3). Lewis acidic and basic sites at typical

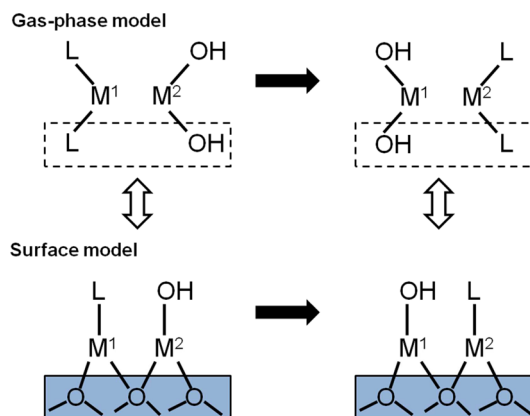


Figure 3. Representations of the gas-phase model (top) for ligand exchange at a surface (bottom).

metal oxide surfaces allow dissociative adsorption of metal complexes¹⁹ and migration of ligands.²⁰ Brønsted elimination of L may then follow from ligands now bound to the original surface metal (M²–L) rather than the incoming precursor. Following the simple model developed for the hydrolysis of ML_q, the free energy change may be calculated for the reaction of M¹L_q with M²(OH)_q [or M²(OH)_q(OH₂)_q for κ_2] resulting in M¹(OH)_q [or M¹(OH)_q(OH₂)_q for κ_2] and M²L_q. In this model the hydroxylated metal complexes represent the metal ions in the oxide surface. All ΔE values are divided by the total number of ligands L, i.e. the product of *p* and *q* in eqs 6a and 6b.

$$\Delta E_{\text{exc}} = \Delta E/(pq):$$

$$pM^1(\kappa_1\text{-L})_q + qM^2(\text{OH})_p \rightarrow pM^1(\text{OH})_q + qM^2(\kappa_1\text{-L})_p \quad (6a)$$

$$\Delta E_{\text{exc}} = \Delta E/(pq): \quad pM^1(\kappa_1\text{-L})_q + qM^2(\text{OH})_p(\text{OH}_2)_p$$

$$\rightarrow pM^1(\text{OH})_q(\text{OH}_2)_q + qM^2(\kappa_1\text{-L})_p \quad (6b)$$

Table 1. Calculated Total Electronic Energies in Atomic Units (E_h) of the Various Spin States of $\text{Mn}(\text{thd})_3$ and $\text{Mn}(\text{OH})_3(\text{OH}_2)_3$ Complexes Using Different DFT Functionals^a

	BP86		PBE		PBE0	
	$\text{Mn}(\text{thd})_3$	$\text{Mn}(\text{OH})_3(\text{OH}_2)_3$	$\text{Mn}(\text{thd})_3$	$\text{Mn}(\text{OH})_3(\text{OH}_2)_3$	$\text{Mn}(\text{thd})_3$	$\text{Mn}(\text{OH})_3(\text{OH}_2)_3$
singlet	-2895.307	-1608.290	-2892.546	-1607.352	-2892.707	-1607.324
triplet	<u>-2895.325</u>	-1608.330	<u>-2892.594</u>	-1607.392	-2892.769	-1607.376
quintet	-2895.314	<u>-1608.368</u>	-2892.583	<u>-1607.433</u>	<u>-2892.784</u>	<u>-1607.431</u>

^aThe energy quoted for the BP86 $\text{Mn}(\text{thd})_3$ singlet is for the spin contaminated form.

When assessing the elimination of L before the ozone pulse, direct elimination by reaction of the M^1L_q precursor with surface hydroxyl groups is considered first using ΔE_{hyd} . If hydrolysis is predicted to be thermodynamically unfavorable or if the ΔE_{hyd} values for two ML_q reactions are similar, then the possibility of ligand exchange between the precursor metal M^1 and surface metal M^2 is considered using ΔE_{exc} . Elimination of L is then reassessed using the ΔE_{hyd} value for M^2L .

2.3. DFT Calculations. The optimized geometries and ground state energies of all reactants and products were determined as isolated molecules in vacuum. DFT calculations were performed using the TURBOMOLE suite of programs.^{21,22} The ground state properties for all species were calculated using the generalized gradient approximation (GGA) density functionals BP86^{23,24} and PBE^{25,26} (with the resolution of identity, RI approximation^{27–29}) and the hybrid functional PBE0^{25,26,30} (sometimes referred to as PBE1PBE). Ahlrich's def2-TZVPP basis sets³¹ were used for all atoms while effective core potentials were applied for the larger Sr, Y, Zr, and La atoms.^{32–34} Calculations were carried out using different DFT functionals to assess the reliability of applying DFT calculated energies to determine the thermodynamic values presented in sections 2.1 and 2.2 above. BP86 was chosen for this work as it had been used previously in a similar study of lanthanum complexes¹⁷ while the other GGA functional PBE was used to investigate the robustness of GGA-type functionals. The hybrid DFT functional PBE0 has been shown to be one of the best performing functionals in calculating reaction energies.^{14,35} Where more than one stable structural isomer was found to exist, the lowest energy isomeric form was determined and selected for the reaction energy calculations.

3. RESULTS AND DISCUSSION

3.1. Electronic State. The spin states of the complexes were varied so as to find the electronic ground state. This showed that most neutral molecular species were closed shell electronic systems, except the Fe and Cu complexes which were found to have doublet ground states, the Cr complexes which had quartet ground states, and the Co and Mn complexes. For the $\text{Co}(\text{OH})_2$ and $\text{Co}(\text{OH})_2(\text{H}_2\text{O})_2$ molecular systems, the quartet ground state was determined to be lowest in energy for calculations using the three DFT functionals used in this work. However, for the calculations using the BP86 and PBE functionals, the energies of doublet ground states of the other CoL_q complexes were found to be lower than those of the quartet. Calculations using PBE0 were consistent with the hydroxylated Co complexes where the quartet state was the lowest energy ground state determined for all CoL_q complexes. For all manganese complexes considered in this work, with the exception of $\text{Mn}(\text{thd})_3$, the quintet ground state with four unpaired electrons was determined using BP86, PBE, and PBE0 functionals to have the lowest energy spin state.

The wave function for $\text{Mn}(\text{thd})_3$ proved difficult to determine using the BP86 functional as no singlet state could be converged to a spin-pure state with the correct occupancy. The application of Fermi orbital shifting³⁶ to an initially singlet state led to significant spin contamination with $\langle S^2 \rangle = 1.010$.

The lowest energy complex with a stable wave function determined for $\text{Mn}(\text{thd})_3$ using this functional was a nonspin-contaminated triplet state with two unpaired electrons while the quintet state with four unpaired electrons had a slightly higher energy (see Table 1).

Calculations using the PBE and PBE0 functionals for all the Mn complexes converged to singlet, triplet, or quintet wave functions without spin contamination. As was found using BP86, for calculations with PBE, the triplet ground state for $\text{Mn}(\text{thd})_3$ was determined to have the lowest energy. For both BP86 and PBE functionals, the quintet state (i.e., four unpaired electrons) of $\text{Mn}(\text{OH})_3(\text{OH}_2)_3$ was the most stable, which was typical for all other MnL_3 complexes except $\text{Mn}(\text{thd})_3$. For the calculations using PBE0, the quintet state had a lower energy than the singlet and triplet ground states for both $\text{Mn}(\text{thd})_3$ and $\text{Mn}(\text{OH})_3(\text{OH}_2)_3$. When calculating the changes in free energy, only energies from Mn and Co complexes with the same spin state were used (e.g., ΔE_{hyd} was calculated for BP86 using the energies of $\text{Mn}(\text{thd})_3$ and $\text{Mn}(\text{OH})_3(\text{OH}_2)_3$ both with $\langle S^2 \rangle = 2$).

3.2. Optimized Geometries. The geometries for the anionic ligand species L^- and corresponding neutral H–L molecules were optimized using DFT methods. The lowest energy forms for the 5 H–L molecules are depicted in Figure 4.

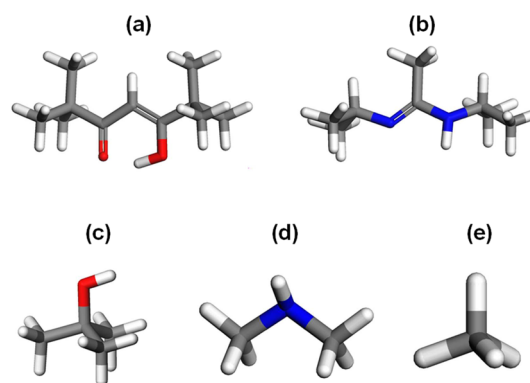


Figure 4. Optimized geometries of neutral H–L species: (a) α -ene β -hydroxy ketone H–thd; (b) di-isopropyl acetamidine (H–amd); (c) *tert*-butanol (H–OtBu); (d) dimethyl amine (H–dma); (e) methane (CH_4). Depictions are not shown to scale.

The enol tautomer of H–thd shown in Figure 4a was found to be lower in energy than both the keto tautomer and alternative enol form with the H atom rotated away from the non-H-bonded carbonyl group in agreement with “ β -diketones” in previous calculations³⁷ and experiments in weakly interacting media.³⁸ Both the H–thd molecule and thd[−] ligand were determined to have a planar “backbone” with the carboxyl and alcohol groups as well as the heptane carbon chain, including the C atoms of the methyl groups trans to the O groups, lying

in one plane. The bulkier methyl group attached to the central C atom of the two amd species (H-amd shown in Figure 4b) was found to interact with the terminal isopropyl groups, distorting the backbone of both the anionic ligand and the neutral molecule slightly out of plane.

The coordination geometry of the complexes containing the bidentate ligands thd and amd were generally very similar. Two different geometrical alignments of the thd and amd ligands were determined for the ML_2 complexes. For $M = Mg, Ca, Sr,$ and Zn , the geometries in the coordination sphere were found to be of D_{2d} symmetry, with the metal bound to the four O/N atoms of the ligands in a distorted tetrahedral arrangement (cf. Figure 5A.III and B.III). The $M(thd)_2$ and $M(amd)_2$ complexes

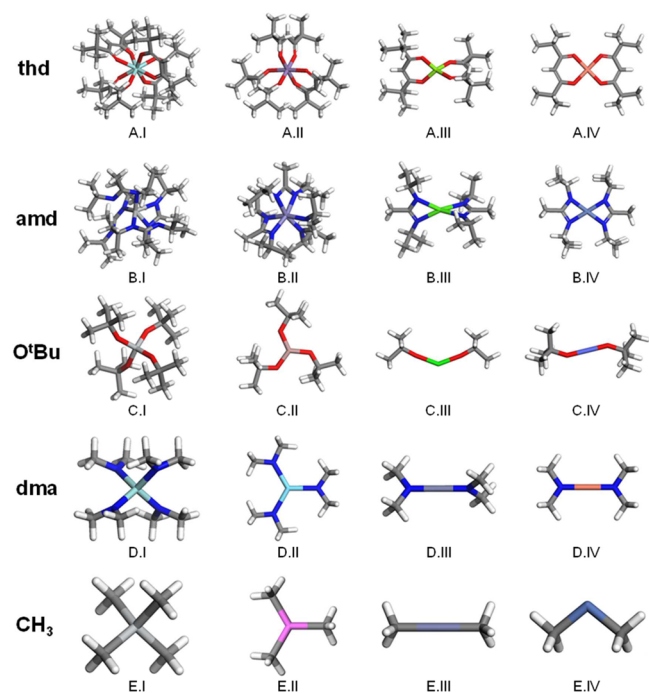


Figure 5. Examples of DFT optimized geometries of $M(L)_q$ complexes determined using PBE0/TZVPP. (A.I–IV) thd complexes of Zr, Mn, Mg, and Cu, respectively; (B.I–IV) Ti, Fe, Ca, and Ni complexes of amd; (C.I–IV) Ti, Ga, Sr, and Co complexes of O'Bu; (D.I–IV) Zr, La, Zn, and Cu complexes of dma; and (E.I–IV) Ti, Al, Zn, and Ni complexes of CH_3 . Gray = C, white = H, red = O, blue = N; metals are various colors. Depictions of the molecules are not shown to scale.

of transition metals ($M = Co, Ni,$ and Cu) have an approximate symmetry of D_{2h} with the four ligand–metal bonds in one plane (cf. Figure 5A.IV and B.IV). The optimized geometries for all $M(thd)_3$ and $M(amd)_3$ molecules, where $M = Sc, Y, La, Mn, Fe, Cr, Al,$ and Ga , were found to be of $\sim C_3$ symmetry with the bulky ligands arranged radially around the metal center and their O atoms approximating an octahedron (cf. Figure 5A.II and B.II). For the $M(thd)_4$ complexes calculated in this work, the central metal ions were coordinated to the ligands in an approximate antiprism geometry (cf. Figure 5A.I). $Zr(amd)_4$ was found to have a similar geometric arrangement of ligands to the $M(thd)_4$ molecule with $Zr-N$ bond lengths of between 2.3 and 2.4 Å. In the structure determined for $Ti(amd)_4$, only one of the amd ligands was bidentate ($Ti-N$ bond lengths of 2.19 and 2.1 Å) with the other 3 ligands monodentate with $Ti-N$ distances of ~ 2.0 and ~ 3.0 Å (cf. Figure 5B.I). This difference in structure between Ti and Zr amd complexes is probably due

to the smaller ionic radius of Ti and the resulting steric hindrance in the ligand sphere. The geometric arrangement of the atoms of the thd ligands were similar to those for the free thd[−] anion while for most the $M(amd)_q$ complexes the atoms exhibited a similar atomic arrangement as the free anion (c.f. H–thd and H–amd in Figure 4). A different atomic arrangement of the amd ligand, where one of the terminal isopropyl groups was rotated by 180° relative to that shown in Figure 4, was found to be the lower energy configuration for the bulkier $Ti(amd)_4$ and $Zr(amd)_4$ complexes and for the $Ni(amd)_2$ complex.

Less steric hindrance and more flexible M–L bonding leads to a greater variety of geometric structures for the monodentate ligand complexes. Of the $M(O^tBu)_2$ complexes, Mg, Co, and Cu have linear O–M–O bonds. Mg, Co, and Cu have C–O–M bond angles of 180°, 149°, and 129°, respectively ($Co(O^tBu)_2$ in Figure 5C.III). Ca, Sr, and $Ni(O^tBu)_2$ are bent, with O–M–O angles of 162°, 139°, and 142°, respectively (Figure 5C.IV), while $Zn(O^tBu)_2$ has a slightly bent O–M–O angle of 172°. Like Mg, Ca and Sr have linear C–O–M bond angles whereas Zn and Ni have C–O–M angles of 124° and 132°, respectively. In all the $M(O^tBu)_3$ complexes, the three O atoms were found to coordinate in a trigonal planar manner, except for $La(O^tBu)_3$ where a O–La–O angle of 114° resulted in a trigonal pyramidal structure. Al and Ga were determined to have bent C–O–M linkages of 136° and 126° in the MO_3 plane (Figure 5C.II), while Fe has an out of plane C–O–M angle of 135°. $Mn(O^tBu)_3$ has a mixture of two in plane C–O–M angles with 139° each, and one out of plane angle of 158°. Sc, Y, and La complexes have linear arrangements of C–O–M. In the Ti and $Zr(O^tBu)_4$ complexes, the O atoms have a tetrahedral coordination structure with C–O–M bond angles of 155° and 180°, respectively (Figure 5C.I).

The seven $M(dma)_2$ complexes were determined to have linear N–M–N bonding, differing between each other in the relative orientation of the two dma ligands. Mg, Ca, Sr, and Zn complexes had an approximate symmetry of D_{2d} where the C–N–C planes of the ligands were at 90° to each other (Figure 5D.III), whereas Co, Cu, and Ni had $\sim D_{2h}$ symmetry with both sets of C–N–C bonds in the same plane (Figure 5D.IV). For all the $M(dma)_3$ complexes, the N atoms were coordinated in a trigonal planar manner to the metal center. For Sc, Y, Al, and Ga, the dma ligands were rotated slightly out of plane with a C_3 point group symmetry. The ligands of $Fe(dma)_3$ were at right angles to the MN_3 plane while in $La(dma)_3$ the ligands were in-plane (Figure 5D.II). $Mn(dma)_3$ was determined to have two ligands at 90° to the coordination plane and 1 ligand in-plane. Ti and $Zr(dma)_4$ were calculated to have geometries with T_d symmetry about the metal.

Five of the $M(CH_3)_2$ complexes considered in this work were found to have geometries of C_{2v} symmetry with Ni, Co, Sr, Cu, and Ca having bent C–M–C bond angles of 103.4°, 110.2°, 114.2°, 130.8°, and 131.1°, respectively. The remaining two $M(CH_3)_2$ complexes with $M = Zn$ and Mg had C–M–C bond angles of 180°. Sc, Y, La, Cr, and Fe had pyramidal geometries with C–M–C bond angles of 118.5°, 110.7°, 105.6°, 112.8°, and 108.4°. Trigonal planar coordination geometries were determined for Al and Ga complexes (C–M–C bond angles of 120°) while the C coordinating atoms of $Mn(CH_3)_3$ were also planar two of the C–Mn–C bond angles were 135° with the third angle 90°. For $Ti(CH_3)_4$ and

Zr(CH₃)₄, the C atoms were coordinated in an ideal tetrahedral arrangement (i.e., C–M–C = 109.5°).

The optimized geometries with the lowest energy isomeric configuration for the hydroxylated metals, M(OH)_q, and the corresponding hydrated species, M(OH)_q(OH₂)_q, were determined for all 17 metallic cations M with charge *q*. For the M(OH)₂ complexes, the O–M–O bond angle was linear for M = Mg, Co, Cu, and Zn while Ca, Sr, and Ni had bent structures with O–M–O angles of 163°, 140°, and 139°, respectively. For the M(OH)₃ molecules, Al, Sc, Mn, and Ga complexes were found to be planar with in-plane bent M–O–H bonds. Y(OH)₃ was also planar but with linear M–O–H bonds. The coordinating O atoms and central M cation for the Fe and Cr hydroxylated complexes were also calculated to be planar but with the terminal H atoms bent out of plane. Unlike the other M(OH)₃ complexes, La(OH)₃ was found to have a slightly pyramidal structure with an O–La–O bond angle of 117°. Ti(OH)₄ and Zr(OH)₄ were found to have similar structures with the O atoms coordinated the central metal with a *T_d* symmetry.

The optimum arrangement of the OH and H₂O groups around the metal centers for the M(OH)₂(OH₂)₂ complexes reflected the pseudoplanar/tetrahedral coordination determined for the respective ML₂ bidentate complexes (i.e., Ca, Sr, Mg, and Zn tetrahedral and Ni, Co, and Cu planar) with hydrogen bonding between the H atom of a water group and the O atom of a hydroxyl. For the geometry optimized M(OH)₃(OH₂)₃ complexes, the O atoms were found to form an approximate octahedron within the coordination sphere with hydrogen bonding between one of the H atoms of the H₂O groups and O atom of the OH ligands, distorting the *O_h* coordination symmetry. The *fac* isomer, where the OH/H₂O ligands are mutually cis, was determined to be the lowest energy isomeric form. The H₂O groups in Ti(OH)₄(H₂O)₄ and Zr(OH)₄(H₂O)₄ were determined to be positioned between pairs of OH ligands where hydrogen bonding was apparent between an H atom of H₂O and an O atom of one OH group and the O atom of H₂O with the H atom of another OH group.

3.3. Brønsted and Lewis Basicity. The Brønsted basicities (eq 4) for the different ligand anions determined using BP86, PBE, and PBE0 functionals are shown in Table 2. For all

Table 2. ΔE_{BB} Values (Equation 4; kJ mol⁻¹) for the Five Ligands Considered in This Work Determined Using Energies Calculated Using BP86, PBE, and PBE0 Functionals and the def2-TZVPP Basis Set

	amd	thd	O ^t Bu	dma	CH ₃
BP86	131.27	222.90	110.17	27.81	-87.45
PBE	136.23	227.60	114.12	31.37	-85.86
PBE0	123.67	222.36	101.22	16.96	-89.27

functionals the same trend in Brønsted basicity was found, which is, in order of increasing basicity, the following: thd > amd > O^tBu > dma > CH₃. Only the very reactive CH₃⁻ ion is predicted to be more basic than OH⁻. Using these values alone, M(CH₃)_q followed by the M(dma)_q complexes are predicted to be the most reactive toward hydrolysis and hence toward ALD. M(O^tBu)_q and M(amd)_q complexes are predicted to have similar reactivity, with O^tBu reactions slightly more exothermic, and the M(thd)_q complexes predicted to be the least reactive. Another general trend seen in these data is the up to 14 kJ

mol⁻¹ difference in ΔE_{BB} calculated using the three functionals with PBE > BP86 > PBE0.

The ΔE_{LB} values determined for the M(thd)_q complexes using BP86, PBE, and PBE0 functionals are shown in Figure 6.

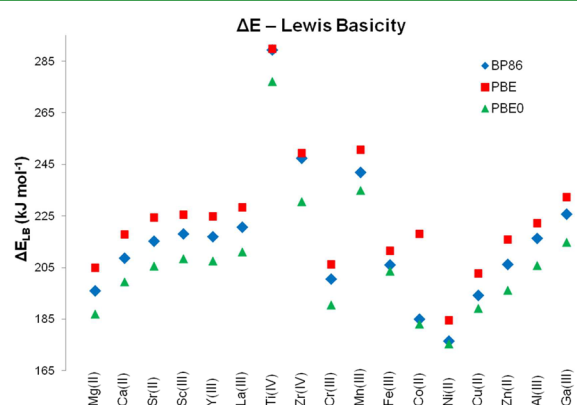


Figure 6. Plot comparing the ΔE_{LB} values determined for M(thd)_q systems (eq 5b). Energies were calculated using the BP86, PBE, and PBE0 functionals and TZVPP basis sets. The ΔE_{LB} values presented here for Mn and Co are for the quintet state and the quartet state respectively and not for the lower energy triplet state for Mn and doublet state for Co found using BP86 and PBE functionals.

These results are shown as an example of the Lewis basicity calculations of L⁻ relative to OH⁻ in forming ML_q and M(OH)_q complexes (eqs 5a and 5b). Similar to the ΔE_{BB} calculations seen above, differences between the ΔE_{LB} values calculated using the three functionals are apparent, where generally PBE > BP86 > PBE0. There are however some M(thd)_q systems that do not follow this trend where with ΔE_{LB} for Ti(thd)₄ and Zr(thd)₄ the BP86 and PBE results are almost identical. These results predict the relative thermodynamics for the hydrolysis of M(thd)_q systems, where more positive ΔE_{LB} values mean that hydrolysis is more favorable and thus mean that thd shows lower Lewis basicity with M. For instance, of the metal cations considered here, thd is the least basic in combination with M = Ti(IV) and most basic with Ni(II). ΔE_{LB} does not take into account the formation of the H–L molecule determined using ΔE_{BB} and therefore cannot alone predict the relative reactivity of ML_q complexes with different ligands L. To do this, one must determine the energy change during the complete hydrolysis, ΔE_{hyd} (eqs 3a and 3b). The ΔE_{LB} results for the other ML_q systems (L = amd, O^tBu, dma, and CH₃) are plotted in Figures S.1–S.4 of the Supporting Information.

3.4. Free-Energy Change for Hydrolysis. One of the main goals of the current work is to assess the reactivity of a metal precursor or fragment with surface hydroxyl groups or water pulses using a simple gas-phase model. We use ΔE_{hyd} as a metric for the elimination of H–L during ALD by reaction between ML_q and OH on the surface (eqs 3a and 3b). Therefore, the absolute values of ΔE_{hyd} have limited significance, but the relative values allow one to compare the reactivity of precursors as a function of metal ion, ligand, and coordination number. The more negative the ΔE_{hyd} value for gas-phase hydrolysis, the more likely the ligand is to be eliminated. Conversely, the higher the relative ΔE_{hyd} value, the more stable the ML_q complex is to hydrolysis and the less likely the ligand is to be eliminated from the surface. From the comparison of the ΔE_{BB} and ΔE_{LB} values above (see Table 2

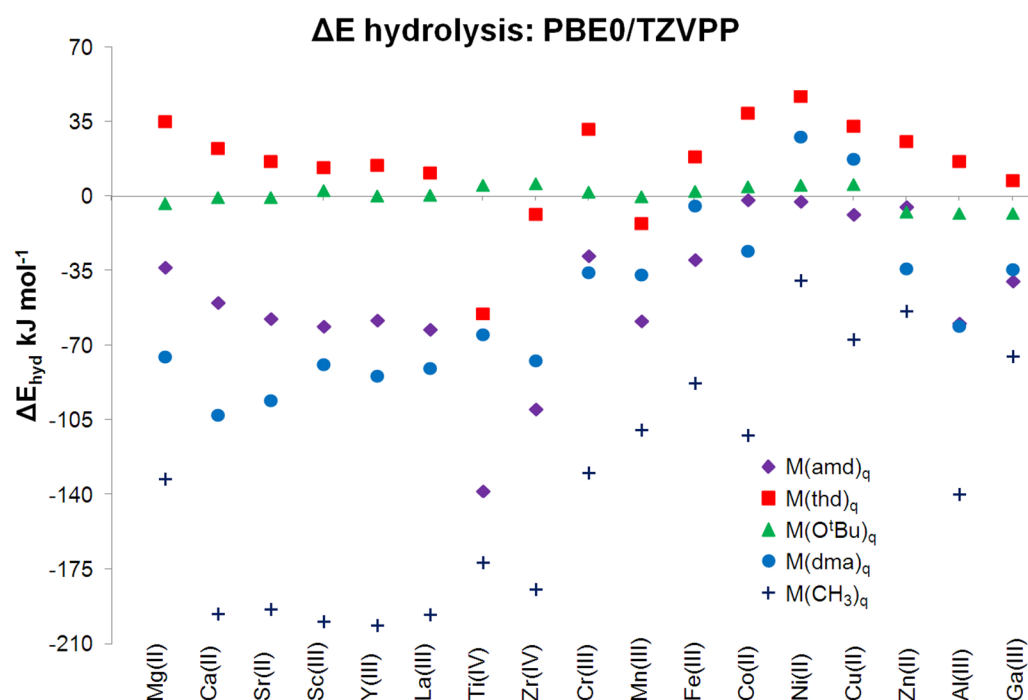


Figure 7. Plot of the DFT calculated energies of hydrolysis (eqs 3a and 3b) for a selection of ML_q ALD precursors. Reactivity toward hydrolysis increases with negative ΔE_{hyd} .

and Figure 6), it has been shown that although the absolute energies calculated using the various DFT functionals are different, the energy trends between the different molecular systems are, with a few exceptions, very similar. These comparable energy trends lead to similar conclusions to be made when considering relative reactivity whether comparing BP86, PBE, or PBE0 results. We do however note that calculations using the PBE0 hybrid functional have compared very well to experimental results as well as other DFT functionals^{14,35} and will therefore be used in evaluating the ΔE_{hyd} results.

As shown in Figure 7, the ΔE_{hyd} values determined for the O-bound ligands (thd and O^tBu) are generally positive or only slightly negative indicating that hydrolysis would be thermodynamically unfavorable. The only negative energy results predicted for the $M(\text{thd})_q$ complexes using the PBE0 functional were those for the hydrolysis of $\text{Ti}(\text{thd})_4$, $\text{Zr}(\text{thd})_4$, and $\text{Mn}(\text{thd})_3$, reflecting ΔE_{LB} (section 3.3, Figure 6). Of the other thd complexes considered here, there is a small difference in the ΔE_{hyd} values, ranging from 7.6 kJ mol^{-1} for Ga(III) to 47.1 kJ mol^{-1} for Ni(II) using molecular energies calculated with PBE0. This relatively small average deviation of 15.5 kJ mol^{-1} from the mean illustrates that the identity of the metal is a relatively minor factor in the case of thd. For the hydrolysis of the $M(\text{O}^t\text{Bu})_q$ complexes, the nature of the metal is of even less importance. The difference between the most endothermic complex Zr(IV) ($\Delta E_{\text{hyd}} = 5.9 \text{ kJ mol}^{-1}$) and exothermic complex Al(III) ($\Delta E_{\text{hyd}} = -7.9 \text{ kJ mol}^{-1}$) is predicted to be only 13.8 kJ mol^{-1} , with a small average deviation of 3.4 kJ mol^{-1} about the mean.

The ΔE_{hyd} values of the N-based complexes $M(\text{dma})_q$ and $M(\text{amd})_q$ were found to be fairly similar. All $M(\text{amd})_q$ hydrolysis reactions are predicted to be negative. $\text{Ni}(\text{dma})_2$ and $\text{Cu}(\text{dma})_2$, with ΔE_{hyd} values of 28.0 and 17.7 kJ mol^{-1} respectively, are calculated to be the only positive $M(\text{dma})_q$ reactivities. This similarity in reactivity between these two

amide ligands was not predicted by the Bronsted base model (ΔE_{BB} , section 3.3, Table 2) and shows the importance of the formation of H–L in the hydrolysis reactions. The $M(\text{CH}_3)_q$ hydrolysis reactions are predicted to be the most exothermic, with all ΔE_{hyd} values negative. There is also a greater range of reactivity predicted for $M(\text{CH}_3)_q$ complexes with an average deviation of 45.1 kJ mol^{-1} from the mean for ΔE_{hyd} , probably reflecting M-specific variations in M–C covalency.

Some trends in reactivity can be extracted from the ΔE_{hyd} values for $M(\text{dma})_q$, $M(\text{amd})_q$, and $M(\text{CH}_3)_q$ complexes (and to a lesser extent in the results for $M(\text{thd})_q$). Hydrolysis of the three group 2 metal complexes is relatively exothermic with a decrease in ΔE_{hyd} going from Mg to Sr. The group 3 metals show comparable reactivity to Ca with very little change going down the group. An increase is seen in ΔE_{hyd} for the transition metals going from group 4 to 9 and 10 where Co or Ni complexes are the least reactive. There is then a decrease in ΔE_{hyd} from group 11 to group 12. Notable outliers in these trends are probably due in the case of Ti and Zr to steric hindrance in the coordination spheres and for Cr and Mn, due to the high spin states of these complexes.

3.5. Ligand Exchange. Due to the large number of ligand exchange reactions possible (mechanism C), a matrix of ΔE_{exc} (eqs 6a and 6b) results was calculated for each of the five groups of ligand complexes. An example of these results is shown in Table 3 for $M^1(\text{thd})_q$ ligand exchange with various $M^2\text{O}_x$ oxide surfaces. From this table, it can be seen that the $\text{Ti}(\text{thd})_4$ and $\text{Zr}(\text{thd})_4$ precursors are predicted to exchange ligands with all $M_2(\text{OH})_q(\text{OH}_2)_q$ complexes to give $M_2(\text{thd})_q$ and $\text{Ti}(\text{OH})_4(\text{H}_2\text{O})_4$ or $\text{Zr}(\text{OH})_4(\text{H}_2\text{O})_4$ due to the inherent instability of these high coordination number molecules (Figures 6 and 7). Conversely, some complexes like $\text{Co}(\text{thd})_2$ and $\text{Ni}(\text{thd})_2$ are very stable and are predicted to exhibit limited ligand exchange with other metal oxide surfaces.

These gas-phase results are interpreted for a surface as follows: we predict that adsorption of $\text{Ti}(\text{thd})_4$ on an M^2 oxide

Table 3. ΔE_{exc} for $L = \text{thd}$ Determined Using $p\text{M}^1\text{L}_q + q\text{M}^2(\text{OH})_p(\text{OH}_2)_p \rightarrow p\text{M}^1(\text{OH})_q(\text{OH}_2)_q + q\text{M}^2\text{L}_p$ (See Equation 6b), Where Metal M_2 Is Shown^a

M_1/M_2	Mg	Ca	Sr	Sc	Y	La	Ti	Zr	Cr	Mn	Fe	Co	Ni	Cu	Zn	Al	Ga
<i>Mg</i>	0.0	-12.5	-18.6	-21.5	-20.5	-24.1	-90.2	-43.6	-3.6	-47.9	-16.7	4.0	11.7	-2.2	-9.2	-18.8	-27.8
<i>Ca</i>	12.5	0.0	-6.1	-9.0	-8.0	-11.6	-77.7	-31.0	9.0	-35.4	-4.2	16.5	24.2	10.4	3.3	-6.3	-15.2
<i>Sr</i>	18.6	6.1	0.0	-2.9	-1.9	-5.5	-71.6	-25.0	15.0	-29.3	1.9	22.6	30.3	16.5	9.4	-0.2	-9.2
<i>Sc</i>	21.5	9.0	2.9	0.0	1.0	-2.6	-68.7	-22.1	17.9	-26.4	4.8	25.5	33.2	19.4	12.3	2.7	-6.3
<i>Y</i>	20.5	8.0	1.9	-1.0	0.0	-3.6	-69.7	-23.1	16.9	-27.4	3.8	24.5	32.2	18.4	11.3	1.7	-7.3
<i>La</i>	24.1	11.6	5.5	2.6	3.6	0.0	-66.1	-19.4	20.6	-23.8	7.4	28.1	35.8	22.0	14.9	5.3	-3.6
<i>Ti</i>	90.2	77.7	71.6	68.7	69.7	66.1	0.0	46.7	86.7	42.3	73.5	94.2	101.9	88.1	81.0	71.4	62.5
<i>Zr</i>	43.6	31.0	25.0	22.1	23.1	19.4	-46.7	0.0	40.0	-4.4	26.9	47.6	55.2	41.4	34.4	24.8	15.8
<i>Cr</i>	3.6	-9.0	-15.0	-17.9	-16.9	-20.6	-86.7	-40.0	0.0	-44.4	-13.1	7.6	15.2	1.4	-5.6	-15.2	-24.2
<i>Mn</i>	47.9	35.4	29.3	26.4	27.4	23.8	-42.3	4.4	44.4	0.0	31.2	51.9	59.6	45.8	38.7	29.1	20.2
<i>Fe</i>	16.7	4.2	-1.9	-4.8	-3.8	-7.4	-73.5	-26.9	13.1	-31.2	0.0	20.7	28.4	14.6	7.5	-2.1	-11.1
<i>Co</i>	-4.0	-16.5	-22.6	-25.5	-24.5	-28.1	-94.2	-47.6	-7.6	-51.9	-20.7	0.0	7.7	-6.1	-13.2	-22.8	-31.8
<i>Ni</i>	-11.7	-24.2	-30.3	-33.2	-32.2	-35.8	-101.9	-55.2	-15.2	-59.6	-28.4	-7.7	0.0	-13.8	-20.9	-30.5	-39.5
<i>Cu</i>	2.2	-10.4	-16.5	-19.4	-18.4	-22.0	-88.1	-41.4	-1.4	-45.8	-14.6	6.1	13.8	0.0	-7.0	-16.7	-25.6
<i>Zn</i>	9.2	-3.3	-9.4	-12.3	-11.3	-14.9	-81.0	-34.4	5.6	-38.7	-7.5	13.2	20.9	7.0	0.0	-9.6	-18.6
<i>Al</i>	18.8	6.3	0.2	-2.7	-1.7	-5.3	-71.4	-24.8	15.2	-29.1	2.1	22.8	30.5	16.7	9.6	0.0	-9.0
<i>Ga</i>	27.8	15.2	9.2	6.3	7.3	3.6	-62.5	-15.8	24.2	-20.2	11.1	31.8	39.5	25.6	18.6	9.0	0.0

^aValues were calculated using molecular energies from PBE0/TZVPP calculations and are in units of kilojoules per mole.

surface will be followed rapidly by migration of thd to exposed M^2 cations and incorporation of the Ti cations into the oxide surface or even subsurface layers. The result is a ternary oxide of Ti and M^2 , covered with a surface of M^2 -thd fragments. On the other hand, $\text{Ni}(\text{thd})_2$ is predicted to retain its ligands after adsorption onto a mixed oxide surface.

Tables for the other ML_q ΔE_{exc} values, where $L = \text{amd}$, O^tBu , dma , and CH_3 , are tabulated in Tables S.1–S.4 of the Supporting Information.

4. DFT MODEL ASSESSMENT OF EXPERIMENTAL COMPOSITIONS

In the following, reaction mechanisms for the growth of ternary oxides predicted the DFT hydrolysis model are assessed through comparison with experimental results found in the literature. Reaction mechanisms A and B (section 1) had been previously proposed in ref 8 from experimental stoichiometries of $\text{M}^1_x\text{M}^2_{1-x}\text{O}_y$ grown by alternating $\text{M}^1(\text{thd})_q$ and $\text{M}^2(\text{thd})_p$ metal precursors in thermal ALD with ozone oxidation. These mechanisms (parts A–E) are re-examined in light of the theoretical results presented above. Experimental results from

other literature sources using different ML_q precursors are also examined in parts F–H.

A. LaMnO_x . For the deposition of LaMnO_x from $\text{La}(\text{thd})_3$, $\text{Mn}(\text{thd})_3$, and O_3 , a good linear fit had been previously⁸ found between both mechanisms and the experimental data (Figure 8). This would indicate that either no H-thd is eliminated before the oxidation pulse following the purely combustion mechanism A or, if elimination of H-thd occurs, thd ligands are transferred from one metal to the other via mechanism C. One possible scenario for mechanism C is the transfer of thd from Mn to La, forming more stable metal–ligand bonds. This mechanism is supported from experiments where the deposition of $\text{Mn}(\text{thd})_3$ without any other metal precursor is not self-limiting but when combined with $\text{La}(\text{thd})_3$ or $\text{Ca}(\text{thd})_2$ provides good ALD growth.³⁹ Indeed, the PBE0 DFT calculations predict that Mn–thd bonds are more labile toward hydrolysis than the La–thd bonds (Figure 7). Hence the exchange model with $\text{M}^1 = \text{Mn}$ and $\text{M}^2 = \text{La}$ yields a value of $\Delta E_{\text{exc}} = -23.8 \text{ kJ mol}^{-1}$ (Table 3). This supports the proposed transfer of ligands from manganese to lanthanum during

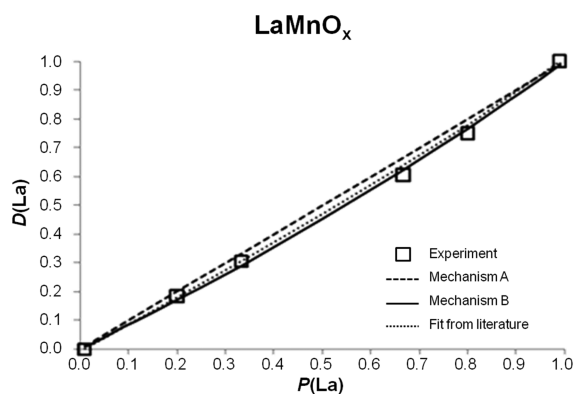


Figure 8. La stoichiometry of LaMnO_x ternary oxide as a function of La ALD pulse ratio.⁸ $D(\text{La})$ is the molar fraction of La deposited relative to the total amount of metal cations, and $P(\text{La})$ is the fraction of $\text{La}(\text{thd})_3 + \text{O}_3$ subcycles relative to the total number of subcycles. The dashed line is a plot of the predicted composition using mechanism A (eq 1), and the solid line is a fit of mechanism B (eq 2) to the experimental data. A previous fit from the literature is represented using the dotted line.³⁹

deposition, so that the surface always consists of $\text{La}(\text{thd})_q$ at the end of either $\text{M}(\text{thd})_q$ pulse.

B. CaMnO_x . A good fit was found between both mechanisms A and B and the experimental data⁸ for CaMnO_x with a nonlinear curve due to the difference in cationic charge: $q_{\text{Mn}} = 3$, $q_{\text{Ca}} = 2$ (Figure 9). Like the deposition of LaMnO_x , it

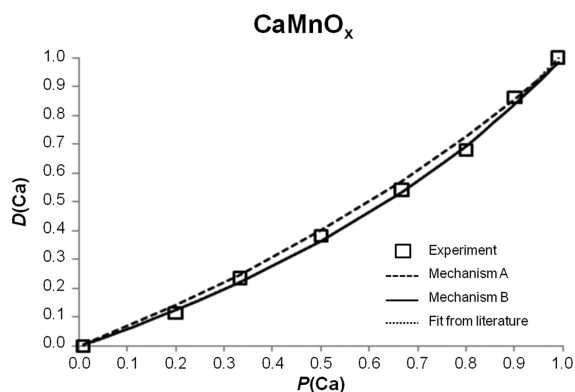


Figure 9. Ca stoichiometry of the CaMnO_x ternary oxide as a function of Ca ALD pulse ratio.⁸ A previous fit of the experimental data³⁹ is obscured by the fit of mechanism B.

is again difficult to distinguish between the two mechanisms. From the DFT calculations, $\text{Mn}(\text{thd})_3$ is predicted to be less stable in the presence of OH groups than $\text{Ca}(\text{thd})_3$ and H–thd elimination is more likely to occur for the Mn complex. However, the computed ΔE_{exc} value of $-35.4 \text{ kJ mol}^{-1}$ for $\text{M}^1 = \text{Mn}$ and $\text{M}^2 = \text{Ca}$ may again confirm the argument for mechanism C, where ligand transfer occurs at the surface from Mn to Ca.

C. CoFeO_x . Again for the deposition of CoFeO_x , it is difficult to distinguish between the two mechanisms, with very similar curves fitting the experimental data (Figure 10). A possible process allowing mechanism B to occur would be a similar reactivity of $\text{Co}(\text{thd})_2$ and $\text{Fe}(\text{thd})_3$ to H–thd elimination. Comparing the energies calculated for the hydrolysis of these two complexes, ΔE_{hyd} for $\text{Co}(\text{thd})_2$ is 20.7 kJ mol^{-1} more positive than that of $\text{Fe}(\text{thd})_3$. Transfer of thd is thus predicted

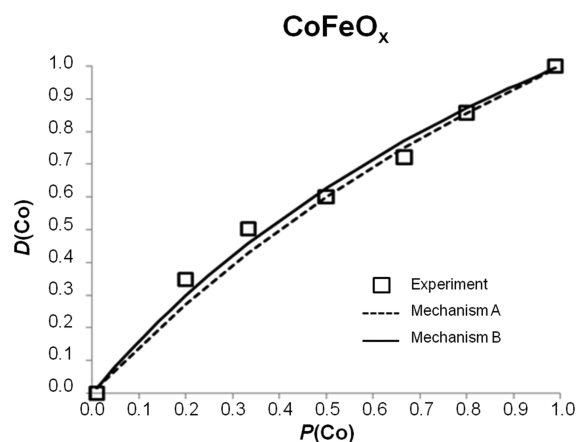


Figure 10. Co stoichiometry of the CoFeO_x ternary oxide as a function of Co ALD pulse ratio.⁸

to take place from the more reactive $\text{Fe}(\text{thd})_3$ complex to the less reactive $\text{Co}(\text{thd})_2$ complex with a ΔE_{exc} value of $-20.7 \text{ kJ mol}^{-1}$. This means that, if mechanism B were in operation, $\text{Fe}(\text{thd})_3$ would be more susceptible to H–thd elimination. However both ΔE_{hyd} values are more positive than those for the group 2 and 3 metal complexes that are predicted to exhibit H–thd elimination. Thus, these gas-phase results may indicate that no Brønsted elimination can occur and that only the combustion type mechanism A is in operation.

D. LaFeO_x . Unlike the previous $\text{M}^1\text{M}^2\text{O}_x$ ALD reactions presented above, there is a clear difference between the fits of the two mechanisms for the deposition of LaFeO_x . Mechanism A predicts a linear relationship between the ratio of La:Fe deposited and the pulse ratio (dashed line Figure 11). This is in

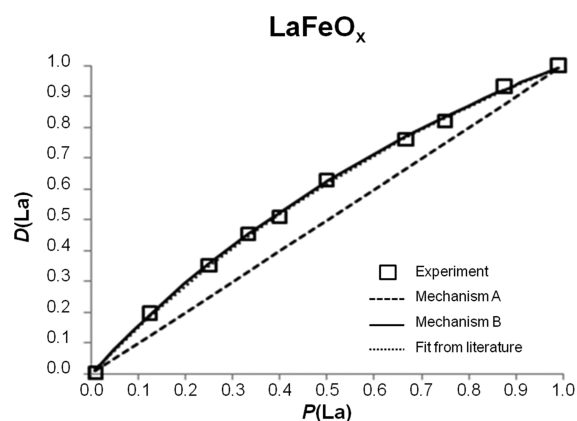


Figure 11. La stoichiometry of the LaFeO_x ternary oxide as a function of La ALD pulse ratio.⁸ The dotted line represents a previous fit to the experimental data⁴⁰ that is almost identical to the fit using mechanism B.

contrast to the near perfect fit of mechanism B with the experimental data⁸ which indicates that the deposition of La is favored over Fe (solid line Figure 11). If mechanism B is correct, La is more reactive to Brønsted elimination of H–thd than Fe. This is supported by the DFT calculated energies where ΔE_{hyd} for $\text{La}(\text{thd})_3$ is lower than that of $\text{Fe}(\text{thd})_3$ but only by 7.4 kJ mol^{-1} per ligand.

E. SrFeO_x . Mechanism A for the deposition of SrFeO_x underestimates the ratio of Sr deposited to that of Fe (dashed line Figure 12). In contrast, mechanism B has an excellent fit to

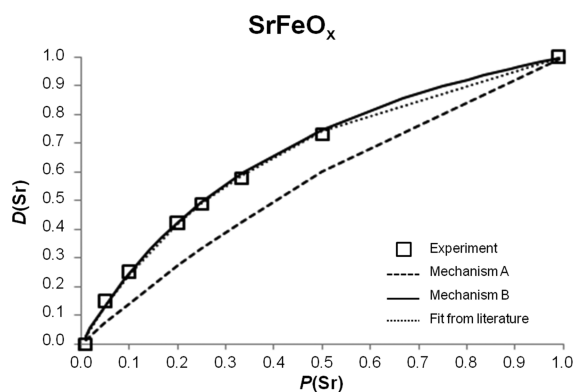


Figure 12. Sr stoichiometry of the SrFeO_x ternary oxide as a function of Sr ALD pulse ratio.⁸ The dotted line represents a previous fit to the experimental data.⁴⁰

the experimental data (solid line Figure 12), similar to that seen for LaFeO_x . The fit of mechanism B to the experimental data appears to indicate elimination of H–thd from the deposition of Sr–thd using up all available OH protons, in contrast to no elimination of H–thd from the deposition of Fe–thd. Looking at the results from the DFT calculations, Brønsted elimination is marginally favored for $\text{Sr}(\text{thd})_2$ by 1.9 kJ mol^{-1} per ligand but not to the same extent as seen in the ALD experiments. Indeed, the difference between the ΔE_{hyd} values for Sr and Fe is not as great as that predicted for La and Fe, which experimentally has a slightly lower ratio of LaO_x in the ALD LaFeO_x thin films than the ratio for SrO_x in SrFeO_x .

F. YScO_x . The stoichiometries of thin films of YScO_x produced using different pulse ratios of $\text{Y}(\text{thd})_3$ and $\text{Sc}(\text{thd})_3$ and O_3 as an oxygen source have been presented by Myllymäki et al.⁴¹ A linear relationship was found between the ratio of metal cations M in the resulting ternary oxide and the ratio of precursor pulses. This would suggest that either mechanism A is in operation, where no H–thd elimination occurs or that if mechanism B is working then $\text{Y}(\text{thd})_3$ and $\text{Sc}(\text{thd})_3$ must have very similar reactivities toward surface OH groups. In the theoretical hydrolysis calculations, $\text{Y}(\text{thd})_3$ and $\text{Sc}(\text{thd})_3$ are seen to have similar ΔE_{hyd} values of 14.9 and 13.9 kJ mol^{-1} , (Figure 7) indicative of the similar reactivity of these group 3 metals.

G. SrTiO_x . SrTiO_x thin films were produced by Kosola et al.⁴² using $\text{Sr}(\text{thd})_2$ and O_3 for the deposition of SrO and $\text{Ti}(\text{t}^{\text{Pr}}\text{O})_4$ and H_2O for the deposition of TiO_2 . The process showed a near linear transfer of pulse ratio to stoichiometry, with for example a Sr:Ti pulse ratio of 1:1 resulting in Sr:Ti atomic ratio in the solid of 0.9. On the other hand, mechanism A predicts that Sr with a smaller charge of +2 would deposit more metal than Ti with a charge of +4 (cf. Figure 1) which according to experiment is not the case. Mechanism B predicts a near linear relationship if the Ti precursor is far more reactive toward Brønsted elimination at the surface and almost no ligands are eliminated from the Sr precursor. In such a scenario, it does not affect the argument whether H_2O or O_3 is used as coreagent prior to the unreactive Sr pulse. Assuming that the reactivity of the iso-propanolate $^{\text{t}}\text{PrO}$ ligands is similar to that of the tert-butanolate $^{\text{t}}\text{BuO}$ ligands, then the computed ΔE_{hyd} value for $\text{Sr}(\text{thd})_2$ is 14.8 kJ mol^{-1} greater than that for $\text{Ti}(\text{t}^{\text{Pr}}\text{O})_4$ (Figure 7) and $\text{Ti}(\text{t}^{\text{Pr}}\text{O})_4$ is predicted to be more reactive than $\text{Sr}(\text{thd})_2$. This supports mechanism B and explains

the experimental finding, although the difference in ΔE_{hyd} is not as great as might be expected from the experimental data.

H. ZnAlO_x . ZnAlO_x ternary oxide films were deposited by Elam and George⁴³ using $\text{Zn}(\text{CH}_2\text{CH}_3)_2$ (DEZ) and $\text{Al}(\text{CH}_3)_3$ (TMA) as metal precursors and H_2O as an oxygen source (not ozone). Our models for ternary oxide stoichiometry have been formulated for the case of well-defined hydroxyl coverage resulting from ozone as oxygen source and so cannot be applied quantitatively in this case. However, the computed energetics can help to interpret the experimental results. At DEZ pulse ratios below 75%, much less ZnO is deposited compared to $\text{AlO}_{3/2}$ than predicted using the “rule of mixtures” (i.e., mechanism A, where the ratio of metal cations in the resulting thin film is dependent only on their charge). Above 75% DEZ pulses, a sharp increase in the relative amount of ZnO deposited is evident, approaching the ratios predicted for mechanism A. ΔE_{hyd} for $\text{Al}(\text{CH}_3)_3$ is computed to be much more exothermic than $\text{Zn}(\text{CH}_3)_2$ (-139.5 vs $-53.6 \text{ kJ mol}^{-1}$, respectively, Figure 7), and it is likely that there is a similar difference between $\text{Al}(\text{CH}_3)_3$ and $\text{Zn}(\text{CH}_2\text{CH}_3)_2$. This large difference in ΔE_{hyd} may indicate that surface reactions as proposed by mechanism B are occurring when pulsing <75% DEZ, with more CH_4 being eliminated from $\text{Al}(\text{CH}_3)_3$ than CH_3CH_3 from DEZ. However, this interpretation mechanism B alone is complicated by an initial loss of mass after the Al precursor pulse of TMA.⁴³ The authors proposed a mechanism for “zinc etching” where the $\text{Al}(\text{CH}_3)_3$ precursor exchanges methyl ligands with the ZnO surface producing the highly volatile $\text{Zn}(\text{CH}_3)_2$ molecule. This mechanism C type reaction is predicted in the current work to be thermodynamically favorable with $\Delta E_{\text{exc}} = -82.6 \text{ kJ mol}^{-1}$ (where $\text{M}^1 = \text{Al}$ and $\text{M}^2 = \text{Zn}$, c.f. Table S.4 in the Supporting Information). Mechanism C would allow the production, followed by desorption, of significant amounts of $\text{Zn}(\text{CH}_3)_2$ (which has a low boiling point of $46 \text{ }^\circ\text{C}$) especially when a ZnO-covered surface is exposed to repeated doses of $\text{Al}(\text{CH}_3)_3$, e.g. for TEZ pulse ratios below 75%.

4.1. Summary of DFT Model Assessment of Experimental Compositions. To summarize the above, no inconsistencies are found between the computed energetic and the experimental data; although in some cases, the magnitude of the observed effect exceeds what the computed value would suggest. In some cases (e.g., LaMnO_x , CaMnO_x), mechanism B can account for the measured stoichiometries as long as ligands are transferred (i.e., mechanism C) to the most acidic metal cations on the surface. Nevertheless, we are still unable to definitively distinguish between mechanism A and B in a few cases (e.g., LaFeO_x , SrFeO_x). This inability of the DFT models to definitively determine the mechanism of growth for some of the $\text{M}^1\text{M}^2\text{O}_x$ solids, in particular for the MFeO_x ternary oxides, highlights some of the problems of using a gas-phase model to represent a reaction at a solid surface. One important factor not considered in the gas-phase models is the acidity of the surface hydroxyl protons. A more acidic $\text{M}^1\text{—OH}$ covered surface would allow more elimination of HL from an incoming M^2L_q precursor, permitting more M^2 ions to be deposited. For example, a relatively more acidic Fe–OH surface would increase the reactivity of precursors toward Brønsted elimination and could explain the increased growth rates of La and Sr ions seen in the deposition of LaFeO_x and SrFeO_x . These differences in surface M–OH reactivities have been previously found to influence the relative deposition rates of Hf and Ti in the ALD of HfTiO ternary oxide thin films.⁴⁴ A more

accurate first principles model would entail calculating the energies for solid slabs of the different oxide surfaces with the precursors placed on the surface.¹⁵ These larger models are of course more time-consuming and difficult to perform, precluding us from the scale of survey presented here (17 metal cations combined with 5 different ligands).

5. CONCLUSION

Our DFT calculations confirm that all metal complexes containing the β -diketonate thd ligand and alkoxide O^tBu are fairly unreactive with respect to elimination of H–thd during ALD. These ligands are removed from the surface through combustion by the coreagent (e.g., ozone or oxygen plasma). The identity of the metal has in most cases a relatively minor effect. However, Ti(thd)₄, Zr(thd)₄, and Mn(thd)₃ have been predicted to be the most reactive of the thd systems studied here toward H–thd elimination.

Amide and amidinate complexes were predicted to show similar reactivity toward hydroxyl groups, with the hydrolysis of most M(amd)_q and M(dma)_q complexes being exothermic. Unsurprisingly, the most reactive complexes toward hydrolysis were determined to be those containing CH₃ ligands. The nature of the central metal cation was found to be more important for the reactivity of M(amd)_q, M(dma)_q, and M(CH₃)_q systems than for M(thd)_q and M(O^tBu)_q.

By modeling the exchange of ligands between different metal cations, the theoretical results have been used to corroborate a ligand transfer mechanism proposed for the deposition of LaMnO_x and CaMnO_x and thus explain the experimentally observed composition of the ternary oxides. Both Co(thd)₂ and Fe(thd)₃ are predicted to be fairly unreactive in ALD, which is consistent with the experimental stoichiometries of CoFeO_x films. La(thd)₃ and Sr(thd)₂ were calculated to be only slightly more reactive to hydrolysis than Fe(thd)₃, and so, we suggest that a more acidic FeOH surface may explain the LaO_x and SrO_x rich films of LaFeO_x and SrFeO_x, respectively, that are observed experimentally. The DFT models developed in this work for metal precursor reactions with growing oxide surfaces successfully predicted the experimental metal cation ratios for many ALD ternary oxides and may be applied to other similar systems, for example, higher order quaternary oxides.

■ ASSOCIATED CONTENT

Supporting Information

Some additional figures and tables are provided, including plots of ΔE_{LB} values and tables of ΔE_{exc} values for four ML_q systems where L = amd, O^tBu, dma, and CH₃. This material is available free of charge via the Internet at <http://pubs.acs.org>.

■ AUTHOR INFORMATION

Corresponding Author

*E-mail: simon.elliott@tyndall.ie.

Notes

The authors declare no competing financial interest.

■ ACKNOWLEDGMENTS

This work was supported by Science Foundation Ireland under the ALDesign project, Grant 09.IN.1.2628, <http://www.tyndall.ie/aldesign>. We would also like to thank O. Nilsen at the Department of Chemistry, University of Oslo, for useful discussions.

■ REFERENCES

- (1) Mitchell, R. H. *Perovskites: Modern and Ancient*; Almaz Press: Ontario, Canada, 2002.
- (2) George, S. M. *Chem. Rev.* **2009**, *110*, 111.
- (3) Kim, H.; Lee, H.-B.-R.; Maeng, W. J. *Thin Solid Films* **2009**, *517*, 2563.
- (4) Leskelä, M.; Ritala, M. *Angew. Chem., Int. Ed.* **2003**, *42*, 5548.
- (5) Niinistö, L.; Nieminen, M.; Päiväsäari, J.; Niinistö, J.; Putkonen, M. *Phys. Status Solidi A* **2004**, *201*, 1443.
- (6) Knez, M.; Nielsch, K.; Niinistö, L. *Adv. Mater.* **2007**, *19*, 3425.
- (7) Seim, H.; Molsa, H.; Nieminen, M.; Fjellvag, H.; Niinistö, L. *J. Mater. Chem.* **1997**, *7*, 449.
- (8) Elliott, S. D.; Nilsen, O. *ECS Trans.* **2011**, *41*, 175.
- (9) Elliott, S. D.; Scarel, G.; Wiemer, C.; Fanciulli, M.; Pavia, G. *Chem. Mater.* **2006**, *18*, 3764.
- (10) Murray, C.; Dozova, N.; McCaffrey, J. G.; FitzGerald, S.; Shafizadeh, N.; Crepin, C. *Phys. Chem. Chem. Phys.* **2010**, *12*, 10406.
- (11) Bühl, M.; Kabrede, H. *J. Chem. Theory Comput.* **2006**, *2*, 1282.
- (12) Waller, M. P.; Braun, H.; Hojdis, N.; Bühl, M. *J. Chem. Theory Comput.* **2007**, *3*, 2234.
- (13) Bühl, M.; Reimann, C.; Pantazis, D. A.; Bredow, T.; Neese, F. *J. Chem. Theory Comput.* **2008**, *4*, 1449.
- (14) Johnson, E. R.; Becke, A. D. *Can. J. Chem.* **2009**, *87*, 1369.
- (15) Elliott, S. D. *Semicond. Sci. Technol.* **2012**, *27*, 074008.
- (16) Holme, T. P.; Prinz, F. B. *J. Phys. Chem. A* **2007**, *111*, 8147.
- (17) Elliott, S. D. *Surf. Coat. Technol.* **2007**, *201*, 9076.
- (18) Kazadojev, I.; Otway, D. J.; Elliott, S. D. *Chem. Vap. Deposition* **2012**, In Press.
- (19) Elliott, S. D.; Greer, J. C. *J. Mater. Chem.* **2004**, *14*, 3246.
- (20) Klejna, S.; Elliott, S. D. *J. Phys. Chem. C* **2011**, *116*, 643.
- (21) *Turbomole, V6.1*; a development of University of Karlsruhe and Forschungszentrum Karlsruhe GmbH, TURBOMOLE GmbH, 2009.
- (22) Ahlrichs, R.; Bär, M.; Häser, M.; Horn, H.; Kölmel, C. *Chem. Phys. Lett.* **1989**, *162*, 165.
- (23) Becke, A. D. *Phys. Rev. A* **1988**, *38*, 3098.
- (24) Perdew, J. P. *Phys. Rev. B* **1986**, *33*, 8822.
- (25) Perdew, J. P.; Burke, K.; Ernzerhof, M. *Phys. Rev. Lett.* **1996**, *77*, 3865.
- (26) Perdew, J. P.; Burke, K.; Ernzerhof, M. *Phys. Rev. Lett.* **1997**, *78*, 1396.
- (27) Eichkorn, K.; Treutler, O.; Öhm, H.; Häser, M.; Ahlrichs, R. *Chem. Phys. Lett.* **1995**, *242*, 652.
- (28) Eichkorn, K.; Weigend, F.; Treutler, O.; Ahlrichs, R. *Theor. Chem. Acc.* **1997**, *97*, 119.
- (29) Sierka, M.; Hogeckamp, A.; Ahlrichs, R. *J. Chem. Phys.* **2003**, *118*, 9136.
- (30) Adamo, C. *J. Chem. Phys.* **1999**, *110*, 6158.
- (31) Weigend, F.; Ahlrichs, R. *Phys. Chem. Chem. Phys.* **2005**, *7*, 3297.
- (32) Kaupp, M.; Schleyer, P. v. R.; Stoll, H.; Preuss, H. *J. Chem. Phys.* **1991**, *94*, 1360.
- (33) Andrae, D.; Häußermann, U.; Dolg, M.; Stoll, H.; Preuß, H. *Theor. Chem. Acc.* **1990**, *77*, 123.
- (34) Dolg, M.; Stoll, H.; Savin, A.; Preuss, H. *Theor. Chem. Acc.* **1989**, *75*, 173.
- (35) Li, S.; Hennigan, J. M.; Dixon, D. A.; Peterson, K. A. *J. Phys. Chem. A* **2009**, *113*, 7861.
- (36) Rabuck, A. D.; Scuseria, G. E. *J. Chem. Phys.* **1999**, *110*, 695.
- (37) Delchev, V. B.; Mikosch, H.; Nikolov, G. S. *Monatsh. Chem.* **2001**, *132*, 339.
- (38) Lozada-Garcia, R. R.; Ceponkus, J.; Chin, W.; Chevalier, M.; Crépin, C. *Chem. Phys. Lett.* **2011**, *504*, 142.
- (39) Nilsen, O.; Rauwel, E.; Fjellvag, H.; Kjekshus, A. *J. Mater. Chem.* **2007**, *17*, 1466.
- (40) Lie, M.; Nilsen, O.; Fjellvag, H.; Kjekshus, A. *Dalton Trans.* **2009**, 481.
- (41) Myllymäki, P.; Nieminen, M.; Niinistö, J.; Putkonen, M.; Kukli, K.; Niinistö, L. *J. Mater. Chem.* **2006**, *16*, 563.
- (42) Kosola, A.; Putkonen, M.; Johansson, L.-S.; Niinistö, L. *Appl. Surf. Sci.* **2003**, *211*, 102.

- (43) Elam, J. W.; George, S. M. *Chem. Mater.* **2003**, *15*, 1020.
- (44) Popovici, M.; Delabie, A.; Van Elshocht, S.; Clima, S.; Pourtois, G.; Nyns, L.; Tomida, K.; Menou, N.; Opsomer, K.; Swerts, J.; Detavernier, C.; Wouters, D.; Kittl, J. A. *J. Electrochem. Soc.* **2009**, *156*, G145.